Dynamic temperature effects in perovskite solar cells and energy yield

Pilar Lopez-Varo, Mohamed Amara, Stefania Cacovich, Arthur Julien, Armelle Yaiche, Mohamed Jouhari, Jean Rousset, Philip Schulz, Jean-Francois Guillemoles, Jean-Baptiste Puel

▶ **To cite this version:**

Pilar Lopez-Varo, Mohamed Amara, Stefania Cacovich, Arthur Julien, Armelle Yaiche, et al.. Dynamic temperature effects in perovskite solar cells and energy yield. Sustainable Energy & Fuels, 2021, 5 (21), pp.5523-5534. 10.1039/d1se01381e . hal-03622152

HAL Id: hal-03622152
https://hal.science/hal-03622152

Submitted on 17 Jul 2022

HAL is a multi-disciplinary open access archive for the deposit and dissemination of scientific research documents, whether they are published or not. The documents may come from teaching and research institutions in France or abroad, or from public or private research centers.

L'archive ouverte pluridisciplinaire **HAL**, est destinée au dépôt et à la diffusion de documents scientifiques de niveau recherche, publiés ou non, émanant des établissements d'enseignement et de recherche français ou étrangers, des laboratoires publics ou privés.

Dynamic Temperature Effects in Perovskite Solar Cells and Energy Yield

Pilar Lopez-Varo,*[a] Mohamed Amara,*[b] Stefania Cacovich,[c] Arthur Julien,[a] Armelle Yaïche,[d] Mohamed Jouhari,[a] Jean Rousset,[d] Philip Schulz,[c] Jean-François Guillemoles,[c] and Jean-Baptiste Puel*[d,a]

Understanding the influence of the temperature on the performance of perovskite solar cells (PSCs) is essential for device optimization and for improving the stability of devices in outdoor conditions. In addition, knowing the transient thermal response of PSCs and the cell temperature to an external agent change (light intensity, temperature, wind speed) is essential to determine the time scales and the span of temperature required in experimental measurement protocols. In this work we study the effect of realistic temperature conditions on the performance of PSCs (cell temperature and efficiency) and their transient response to environmental external changes using a theoretical-experimental combined approach. A thermal transient resistor-capacitor (RC) circuit model, previously developed and validated for silicon photovoltaic modules, is adapted to estimate the cell temperature and to simulate the transient thermal performance of the perovskite solar cell as a function of device parameters and environmental variables. This model considers absorption, convection, conduction, radiative exchanges and it is based on the experimentally measured thermal and optical dependence of electrical parameters of PSCs, strengthening its capacities to predict and optimize the performance of this type of solar cells. We measure the current-voltage (*I-V*) curves as a function of the temperature and light intensities and extract its characteristic *I-V* parameters. By combining the experimental results with our model, we conclude that the increase of the cell temperature is strongly linked to the absorption in the perovskite layer, in the front glass and fluorine doped tin oxide FTO layer. We also analyze the annual energy yield (EY) of stable PSC modules, assuming no device degradation and working on different geographical locations, in PV farms and on rooftops to evaluate the impact of radiative exchange and air convection on the EY. We emphasize the importance of employing a comprehensive thermal model for EY estimations as it can change the results by more than 10 %. The proper calculation of the cell temperature is essential not only to calculate the EY, but also as an input to predict the lifetime of the device. This work opens the possibility to optimize the device from three perspectives: optical, electrical and thermal (stability).

Introduction

Since perovskite solar cells (PSCs) burst into the photovoltaic world, they have attracted huge interest in the scientific community. This is thanks to their unique structural and optoelectronic properties, the low production cost, and the steep growth of their power conversion efficiency[1-3]. The unique electro-optical properties of perovskites include a tuneable direct band gap, a high absorption coefficient, the absence of parasitic sub-band gap absorption (sharp absorption edge), high carrier mobility (10-30 cm^2/Vs), long diffusion length (100 nm - 1 µm), photon recycling, and high defect tolerance[4]. However, despite rapid advances in device performance and without considering the fundamental thermodynamic efficiency limits of PSCs[5], today the main hurdles towards large-scale industrialization of PSCs are the scalability of the fabrication processes and the stability of the PV device under operational condition[6, 7]. In general, the characterization of solar cells is carried out under standard test conditions (STCs), namely, at room temperature, *i.e.* 25 °C, and 1000 W/m^2 of irradiation with an AM 1.5G spectrum. However, the performance of a solar cell deployed in the field differs from the one measured in the laboratory. In reality, solar cells operate under varying meteorological conditions, which comprise a range of different light intensities, spectral distributions, temperatures, chemical

[a] *Institut Photovoltaïque d'Île-de-France (IPVF), 18 Boulevard Thomas Gobert, Palaiseau, 91120, France. E-mail : pilar.lopez-varo@ipvf.fr*

[b] *Université de Lyon, INL-UMR 5270, CNRS, INSA-Lyon, Lyon, 69621, France. E-mail : mohamed.amara@insa-lyon.fr*

[c] *CNRS, Institut Photovoltaïque d'Île-de-France, UMR 9006, 18 Boulevard Thomas Gobert, Palaiseau, 91120, France.*

[d] *Électricité de France, EDF, R&D, 18 Boulevard Thomas Gobert, Palaiseau, 91120, France. E-mail : jean-baptiste.puel@edf.fr*

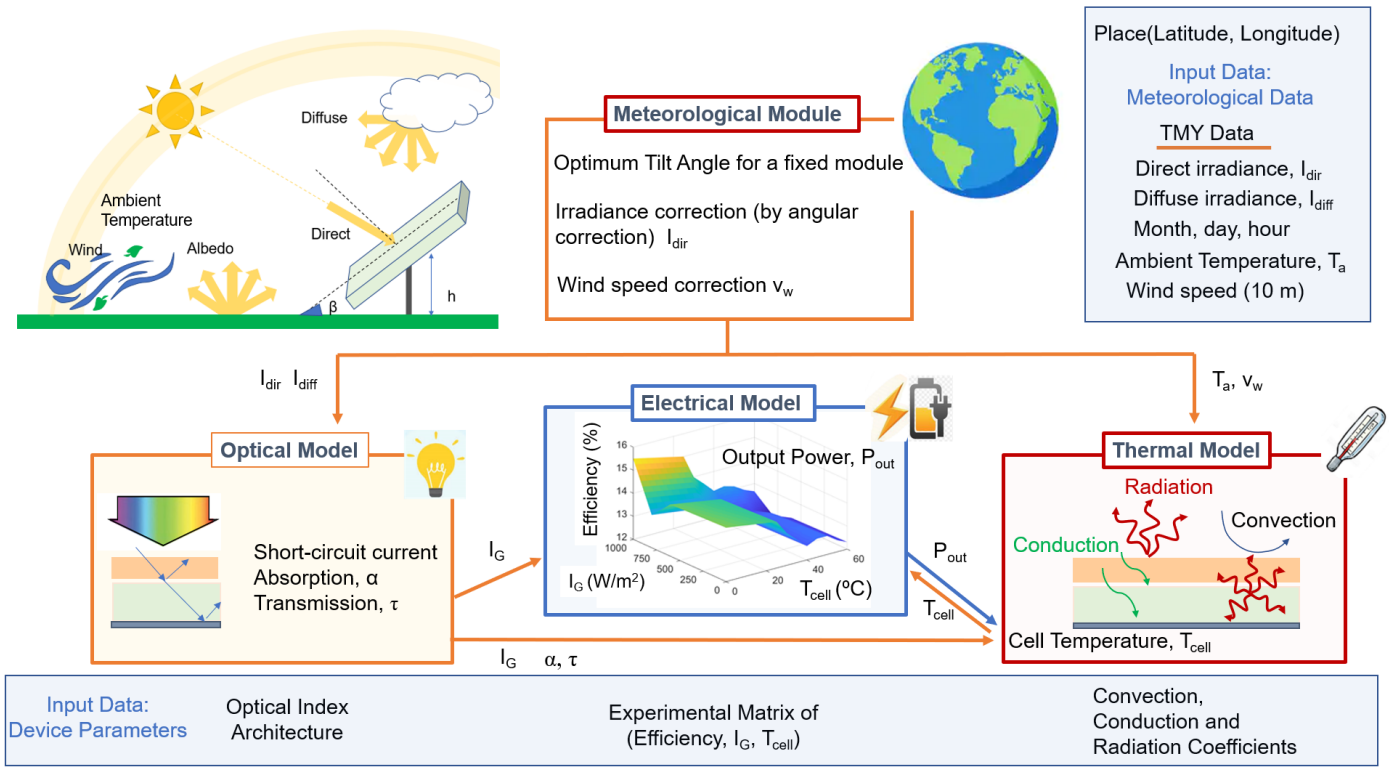

FIGURE. 1. SCHEMATIC OF THE SOFTWARE MODULES.

species, cloud cover, wind speed and humidity[7-10]. In fact, the influence of several factors such as air[11], oxygen[12], humidity[13], light and temperature[14] on the evolution of the performance of the perovskite solar cells is still under debate[15-19]. The change of all these operational and meteorological factors throughout the hours of the day all over the year at each specific location influences both stability and annual energy yield, which is the key quantity to optimize the design of the solar cells[20].

The annual energy yield (EY), defined as the output energy produced by a photovoltaic (PV) system in one year, has been estimated by linking simplistic electrical models with optical models employing realistic irradiance data, or with meteorological data/models[21-24]. To analyze the performance of PSCs under outdoor conditions, several groups have investigated the evolution of current-voltage (*I-V*) characteristics of single-cation halide perovskite solar cells under different temperatures[25-28] and at different light intensities[28]. A clear challenge observed by authors[25, 27, 28] is the change in the optoelectronic properties of PSCs due to structural phase transitions. Methylammonium lead iodide ($CH_3NH_3PbI_3$, $MAPbI_3$) perovskite presents two phase transitions and one of them takes place under realistic work conditions (310 K). In contrast to $MAPbI_3$, triple-cation perovskites have shown this phase transition at temperatures higher than 420 K[29]. Several studies have shown that the carrier transport does not limit the device performance at medium-high temperatures[15, 30]. However, the transport properties are also affected by ion migration, which has been proven to be temperature-dependent.[31] The optical properties of perovskites, which are of significant interest in photovoltaics for the optimization of the device design, have also been analyzed as a function of temperature[32]. Unlike most semiconductors, the band gap increases weakly with the temperature[25, 28]. Green et al.[33] presented an extensive work on the temperature dependence of optical properties.

In PSCs, the interfaces are a weak link with respect to reversible and non-reversible degradation. Temperature-dependent performance changes have also been attributed to variations in the distortion of the perovskite unit cell, which influence the device hysteresis. Investigations on the temperature-dependent hysteresis show that changes in interface properties and selective contact transport layer mobility modify the perovskite solar cell performance.[34] In addition, PSCs are constituted by different organic and inorganic layers. Thus, the temperature dependence of a PSC is not only the temperature dependence of the perovskite layer but also the temperature dependence of each layer and each interface. For example, the typical hole transport layer (HTL) 2,2',7,7'-tetrakis[N,N-di(4-methoxyphenyl)amino]-9,9' spirobifluorene (spiro-OMeTAD) exhibits temperature-activated charge transport properties, and its stability can be dependent on the additives used to improve its conductivity[35-37]. The use of additives can decrease the glass transition temperature (~100 °C) of the intrinsic Spiro-OMeTAD to operational outdoor temperatures (72 °C)[38,39] and create voids.

Recently, Tress et al.[40] presented an extensive experimental analysis of the performance of a triple cation double-halide perovskite solar cell under simulated temperature-illumination real-world operating conditions. They concluded that triple cation PSCs present only a minor decrease of efficiency with elevated temperature and low light intensity, maintaining almost optimum values for typical environmental conditions in

the center of Europe. Recently, M. Jošt et al.[41] measured p-i-n PSCs under realistic outdoor conditions in the laboratory and on the rooftop. Pursuing the same objective, Leong et al.[28] studied the effect of the temperature and illumination on the performance of PSCs by analyzing the experimental response of the solar cell parameters (open-circuit voltage V_{oc}, short-circuit current density J_{sc}, fill-factor FF and power conversion efficiency η). These temperature dependent studies are crucial to predict the performance of PSCs and their EY. Recently, several authors wrote a consensus statement on how to properly perform stability measurements on PSCs[6]. This consensus reinforces the urge to know what the operating temperature is, what is the maximum temperature and, in that way, to set the temperature-dependent measurements. This is due to the fact that higher temperatures accelerate any degradation mechanism in perovskite devices[29, 42, 43]. For example, irreversible optical and electrical degradation was observed at temperatures higher than 70 °C, due to an increase of trapping rates and interfacial degradation by ion migration[44,45].

For numerical analysis, different authors [41, 40] provide a linear expression associating cell temperature to global irradiance and air temperature. However, a robust thermal-electrical-optical model that is (i) a function of the material properties, (ii) self-consistent, based on experimental characteristics of the performance of the PSCs, and (iii) dependent on meteorological data is still missing. In that way, it would be possible to optimize the device from three perspectives: optical, electrical, and thermal (stability). This coupled model would allow the calculation of the operational temperature of these devices which is essential to optimize their efficiency and stability.

From all of that, providing a robust semi-empirical electro-optical and thermal model is the objective of this work (schematic in Fig. 1). The link between experimental data and the theoretical model allows us to evaluate and predict the annual energy yield EY, here however without considering irreversible degradation. To achieve this goal, in the second section, a detailed explanation of the thermal-optical-electrical model is provided. A comprehensive thermal RC model previously proposed for Si-SCs is extended to PSCs[10] taking into account the essential thermal transfer mechanisms that take place in a solar cell. We then combine this model with an opto-electrical model to describe the complete performance of a PSC. In the third section, we present the parameters from the *I-V* characteristics acquired as a function of temperature and light intensity to elaborate a matrix of the irradiance- and temperature dependent efficiency at maximum power output (MPP) of each cell. Finally, in the fourth section, we evaluate the energy yield in different regions, on the rooftop and in a PV farm to study the main physical parameters, which affect the annual EY. In the scope of our model, we investigate the temperature dependence of the device characteristics. Note that elevated temperatures also affect perovskite degradation, which we do not include in our model. Nowadays, there is no clear and unique degradation pathway identified for any given PSC. Nevertheless, as mentioned before, generally any degradation mechanism is thermally activated, therefore, knowing the thermal history is critical to predict degradation. This work contributes to a more realistic assessment of the thermal cycling of the device as a prerequisite to including comprehensive degradation models, EY and levelized cost energy LCOE calculations. We refer the interested readers to further literature on perovskite stability[46] (see more information in section SI S4 about thermal degradation).

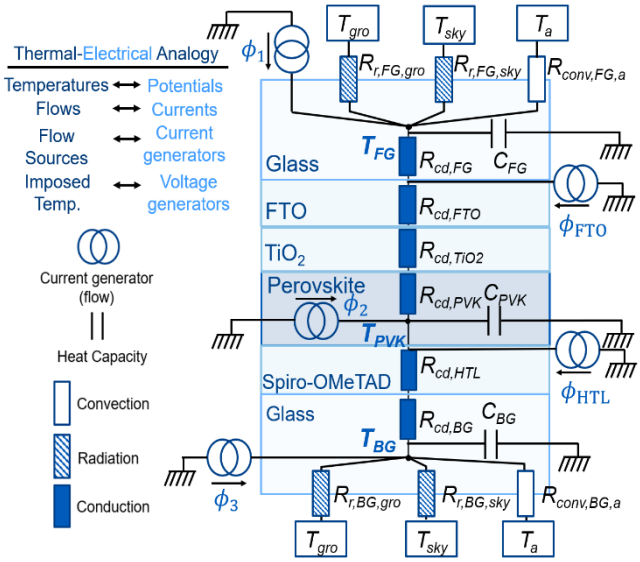

FIGURE. 2. STRUCTURE OF THE PEROVSKITE SOLAR CELL (GLASS/FTO/TiO_2/PEROVSKITE/SPIRO-OMETAD/AU/GLASS) AND RC

2. Thermal-Optical-Electrical Model

Our physical and numerical simulations of the performance of PSCs are based on four software modules (see Fig. 1):

(i) The **Thermal Module** is based on the RC circuit thermal model proposed in this work. In this module, the cell temperature is calculated by means of conduction, absorption, radiation, and convection. The inputs are the meteorological data (ambient temperature, wind speed, direct and diffuse irradiance), the electrical power (which is the output of the Electrical Module (iv)), the optical absorption in each layer (which is the output of the Optical Module (iii)), and the thermal properties and material constants of the device. In this section, we will mainly focus on the description of this module, a detailed derivation is provided in the supplementary information (SI).

(ii) The input for the **Meteorological Module** is the meteorological data from a Typical Meteorological Year (TMY) data base (direct irradiance, diffuse irradiance, wind speed at 10 m above the ground level and ambient temperature) from the Photovoltaic Geographical System of the European Commission[47]. The magnitude of the direct irradiance is corrected for fixed tilted PV modules, while the wind speed is corrected according to the height of the solar PV module with respect to ground level. In this module, we calculate the optimum tilt angle depending on the geographical location of the PV module.

(iii) In the **Optical Module** we use SunSolveTM from PVLighthouse Software for optical simulations to calculate the

total percentage of absorbed, reflected (considering also re-emission) and transmitted irradiance in each layer (see the calculated values in Table 1).[48] The inputs are the device geometry and the refractive indices measured in our laboratory.[49]

(iv) The part of the solar radiation, which is absorbed by the solar cell and not converted into electricity, increases the cell temperature. The Electrical Module determines the extracted output electrical power of the solar cell working under fixed irradiance (output of the Meteorological Module) and fixed cell temperature (output of the Thermal Module). In this module, we consider an empirical matrix of efficiencies for a solar cell working at MPP measured under different irradiance and temperature conditions (Section S2.5 in SI).

2.1 Thermal module: RC Circuit Thermal Model

Different models to evaluate the temperature of silicon solar modules have been proposed in literature[10, 44, 50-56]. These models either focus on the coupling of semiconductor properties,[53-55, 57] accurate calculation of transients for short thermal response times, [10, 58] or simple-steady state conditions considering environmental effects[52].

In this work, we employ a resistor-capacitor RC circuit thermal model which was previously developed and validated for silicon PV modules[10]. The model takes the following essential thermal mechanisms into consideration: absorption (a), conduction (cd), convection (cv) and radiation (r). The model has been developed as an analogy to electric circuit models where temperatures, heat flows, flow sources and imposed temperatures are respectively translated from potentials, currents, current generators and voltage generators. This analogy allows to easily modify this model to be applied on different PV architectures and encapsulant configurations which may impact in the device temperature[59, 60]. We simulated an encapsulated PSC with the following layer stack (see Fig. 2): a front glass (FG) layer, a fluorine doped tin oxide (FTO) electrode, a titanium oxide (TiO_2) electron transport layer, a perovskite absorber layer (PVK), a Spiro-OMeTAD HTL and a back glass (BG) slide. Furthermore, a gold contact layer is placed between the HTL and the BG, which is a good heat conductor and thus simulated as a wire for thermal flows. For the evaluation of the temperature of the perovskite layer T_{PVK}, the front glass T_{FG}, and the back glass T_{BG}, thermal energy balance considering the absorption in each layer as well as radiative, convective and conductive exchanges between the nodes and with the environment are considered. The temperature in the perovskite layer is given by the balance between the energy absorbed in the perovskite layer within a unit of time and the thermal power exchanged by conduction between the perovskite and the adjacent layers towards the front and back glass:

$$C'_{PVK}\frac{dT_{PVK}}{dt} = G_{cd,PVK,FG}(T_{FG} - T_{PVK}) + \quad (1)$$

$$+G_{cd,PVK,BG}(T_{BG} - T_{PVK}) + (\phi_2 + \phi_{HTL})S_{PVK}$$

$$C'_{PVK} = \rho_{PVK}S_{PVK}d_{PVK}C_{PVK}$$

where $G_{cd,i,j}$ is the equivalent thermal conductance (cd) from the series resistances from layer i to layer j. ϕ_2, S_{PVK}, ρ_{PVK}, d_{PVK} and C_{PVK} denote the thermal energy flux absorbed per unit area by the perovskite, the surface, the density, the thickness and the thermal capacitance of the perovskite layer, respectively. The effective thermal capacitance in the perovskite is negligible due to its lesser thickness (400 nm) compared to glass (3 mm). The temperature in the FG and BG layers is given by solving the balance equations:

$$C'_{FG}\frac{dT_{FG}}{dt} = G_{cv,FG,a}(T_a - T_{FG}) + G_{r,FG,sky}(T_{sky} - T_{FG}) + \quad (2)$$

$$+G_{r,FG,gro}(T_{gro} - T_{FG}) + G_{cd,FG,PVK}(T_{PVK} - T_{FG})$$

$$+\phi_{1,3}S_{FG},$$

$$C'_{FG} = \rho_{FG}S_{FG}e_{FG}C_{FG}$$

where G_{cv} is the convective exchange coefficient, T_A is the external ambient temperature, $\phi_{1,3}$ is the thermal energy flux

TABLE 1. LAYER THICKNESSES AND THERMAL PARAMETERS USED IN THE SIMULATIONS OF THE THERMAL MODULE. TRANSMITTED AND ABSORPTION CALCULATED IN THE OPTICAL MODULE.

Material	Thickness, *d*	Thermal Conductivity Λ (W/m/K)	Material Density ρ (kg/m³)	Specific heat Capacitance *C* (J/kg/K) [61]	Capacitive Contribution *C'* (J/K/m²)	Transmission (%)	Absorption, A (%)
Glass FS	1-3.2 mm	1-1.8 [61]	2400-2800 [62]	750-840	1800-7056	83 [19],[63]	9.1
FTO	750 nm	9-98, 31.38 [61]	5560 [61]	343	14.30		9.3
TiO_2	190 nm	8.79 - 13.39 [61]	4250 [61]	686	0.55	-	0.3
Perovskite	400 nm	0.30-0.52 [64]	4000 [62],[65]	322.55	0.43	-	45.5

Spiro-OMeTAD	360 nm	0.1-0.4 [66]	1030 [67]	-	-	-	3.4
Gold	100 nm	317.98 [61]	19290 [62]	128	0.25	0	1.2
Glass BS	1-3.2 mm	1-1.8 [61]	2400-2800 [62]	750-840	1800-7056	0	0

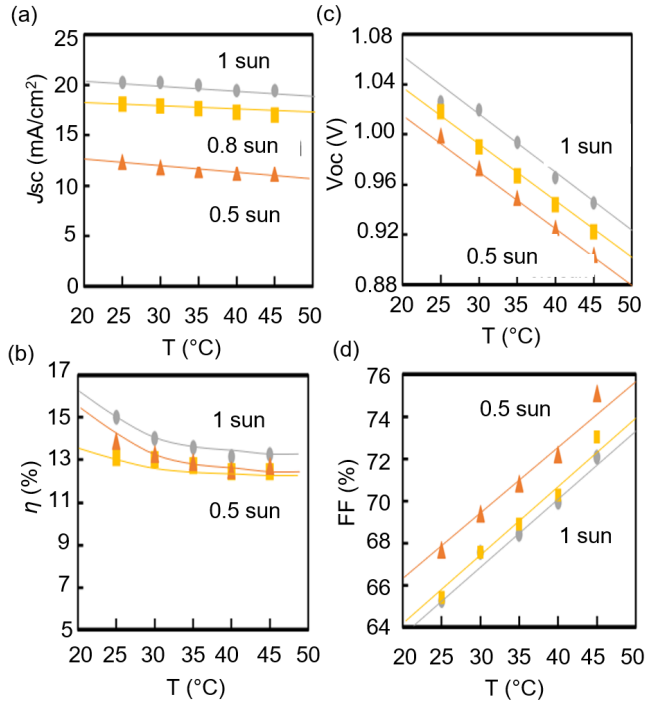

FIGURE. 3. (A)-(D) V_{oc}, J_{sc}, *FF* AND *H* AS A FUNCTION OF THE TEMPERATURE AND AS A FUNCTION OF THE LIGHT INTENSITY FOR THE FORWARD SCAN.

absorbed, $S_{FG,BG}$ is the surface area, $\rho_{FG,BG}$ is the density, $d_{FG,BG}$ is the thickness and C_{FG} and C_{BG} are the thermal capacitance of the FG and BG, respectively. In this equation, the energy accumulated in the FG (BG) by unity of time is equal to the thermal power exchanged by convection between the glass and the surrounding air, by radiation between the glass and the sky and by radiation between the glass and the ground, the thermal power exchanged by conduction between the glass and the perovskite and the thermal power absorbed by the glass ($\phi_{1,3}\ S_{FG,BG}$). All the parameters used in the model are summarized in Table 1. In PSCs, the glass is the thickest layer, thus, the transient thermal response of PSC will be limited by the thermal response of the glass. Most importantly, the increase of the cell temperature is linked to the irradiation absorbed by each layer. In the optical module, we estimate that the percentage of the optical absorption with respect to the total incoming flux is about 45.5-50 % for the perovskite layer (depending on the perovskite composition and the interfacial and glass layers), 9.1 % for the front glass, and 9.3% for the FTO layer. In the case of the perovskite layer, the effective fraction of the absorbed input flux, which contributes to increasing the cell temperature, depends on the operational point, since part of the absorbed energy will be converted into electrical current and extracted. Therefore, if the PSC efficiency is 20 %, between 25.5-30 % of the incoming flux that is absorbed, but not converted into electricity, increasing the cell temperature. The thermal energy flux absorbed by the perovskite, ϕ_2 in eq. (1), is the difference between the absorbed irradiance power and the extracted electrical power. When no electrical power is extracted (at V_{oc} or J_{sc}), all the absorbed energy contributes to heating of the cell, which leads to the solar cell operating at a higher temperature than at the MPP.

3. Experimental Data

As previously mentioned, in this work, we consider the empirical matrix to model the thermal and optical dependence of the electrical performance of the PSCs (Electrical Module, Section 2). In order to build the empirical matrix, we measure the performance parameters, i.e. V_{oc}, J_{sc}, *FF*, and η, of a triple cation perovskite solar cell as a function of temperature and light intensity in air and under vacuum[63]. The complete encapsulated device structure is glass/FTO/c-TiO_2/m-TiO_2/perovskite/Spiro-OMeTAD/Au/glass corresponding to the model device in the simulations.

The characterized PSCs present efficiencies ranging from 15 % to 18 % under STC and low hysteresis in *I-V* curves at room temperature. Further details on the vacuum setup for sample characterization can be found in a previously published report.[68] Without the glass encapsulation we expect additional irreversible degradation due to migration of elemental species in the layer stack or electro-chemical reactions[69] and we indeed observed a significant irreversible deterioration of the short-circuit current in unencapsulated test devices (see Fig. S8 in S2.3 in the SI). We employ the following procedure for testing: **(1) Light soaking:** We let the devices undergo light soaking under 1 sun at room temperature while being held at V_{oc} for 20-30 min to passivate trap states and mitigate initial transient behaviour of the cell characteristics. **(2) Electrical measurements in dark:** Once the cell has reached a constant V_{oc} under light, we measure a dark *I-V* curve (at a low scan rate of 20 mV/s) in reverse and forward bias. **(3) Electrical measurement under illumination:** We switch on the light and keep the cell at open circuit conditions and room temperature (20 °C controlled by a chiller). For each measurement, we wait until the sample reaches thermal equilibrium, normally 1 or 3 min depending on the glass thickness (see SI S2.1). After that, an *I-V* curve is acquired under reverse and forward bias, and for different light intensities. **(4) Temperature ramp in the dark:** the temperature of the device is increased in steps of 5°C every 5 or 10 min for the samples with a glass thickness of 1 mm or 3 mm, respectively. After increasing the cell temperature to 55 °C, we cool the cell (using steps as in the heating sequence) and measure *I-V* curves. The matching of the *I-V* curve parameters

obtained in both heating and cooling sequences confirms that the encapsulated cells did not degrade during the measurements. Further details on the experimental procedures and precautions taken can be found in the SI in section S2. To fully cover the practical working condition, the device characteristic analysis in the temperature range of -20°C to 85°C is suitable to be considered.

In the following discussion, we explore the device functionality as a function of temperature and the corresponding impact of ion migration. In Fig. 3, we show V_{oc}, J_{sc}, *FF* and η as a function of temperature (25-45 °C) and light intensity (1, 0.8 and 0.5 suns) for the sample S1 (Glass/FTO/c-TiO_2/m-TiO_2/Perovskite/Spiro-OMeTAD/Au/Glass). We observe that with increasing temperature the V_{OC} decreases linearly, while the *FF* increases and J_{SC} remains constant. The temperature-dependent evolution of a given *I-V* parameter *X* (J_{sc}, V_{oc}, *FF or* η) can be expressed by the temperature coefficient β_X defined for each parameter *X* as follows[53]:

$$\beta_X(T_c) = \frac{100}{X(25\,°C)} \frac{X(T_c) - X(25\,°C)}{T_c - 25} \left[\frac{\%}{°C}\right] \quad (3)$$

Generally, the coefficient β_X changes with temperature[28] and further depends on device architecture and measurement protocol[25, 41]. In Table 2, we summarize the temperature coefficient for the V_{oc} and for the efficiency, obtained in the literature and this work. The V_{oc} of the PSCs decreases with temperature[17] as observed in other types of solar cells[70]. The physical interpretation of V_{oc} can be expressed as a result of the balance between carrier generation and recombination mechanisms. The generation profile is not significantly affected by the temperature. Therefore, the decrease of V_{oc} with increasing temperature is due to entropic effects (charge carriers access to the density of states in the conduction and valence band[5]), an increase of bulk/surface recombination current at higher temperatures (see SI S2.6), and a variation of the built-in voltage due to ion migration[17].

In particular, a smaller V_{oc} at higher temperature can be correlated to the activation energy of ionic conductivity. For the solar cells based on triple-cation mixed halide perovskite absorbers used here, we observed an increase of the hysteresis in the experimental *I-V* curves at higher temperatures.

In addition, we compared the V_{oc} decays at different temperatures (Fig. S10 in SI2.4) and observed a slower decay at lower temperatures than the ones at higher temperature, which is consistent with previously reported data.[71] From these two experimental observations, we can conclude an increase of ion migration at higher temperature in our samples.

TABLE 2. TEMPERATURE COEFFICIENTS FOR V_{oc} AND EFFICIENCY FROM ROOM TO HIGHER TEMPERATURES.

β_X	Architecture	Value
β_{Voc}	Glass/FTO/TiO_2/perovskite/Spiro-OMeTAD/Au/glass (this work)	-0.31 - -0.11 %/°C
	Glass/ITO/TiO_2/ $MAPbI_3$/ Spiro-OMeTAD/Au [17]	-0.12 - -0.09 %/°C
	Dupré et al. [25] (different structures)	-0.29 - -0.19 %/°C
	[18] (tested under Temperature cycling)	-0.11 %/°C
β_η	Detailed Limit Balance [41]	-0.13 %/°C
	glass/ITO/MeO-2PACz/perovskite/C_{60}/SnO_2/Cu. [41] (η = 18.3 %, tested by *I-V* curves and under temperature cycling)	-0.17%/°C and -0.22%/°C (25 °C > T > 80 °C)
	Semi-transparent p–i–n stack.[72]	-0.18%/°C
	Glass/FTO/TiO_2/ perovskite / Spiro-OMeTAD/Au/glass (this work)	-0.46- -0.3 %/°C (T > 20 °C)
	Dupré et al. [25]	-0.8 - -0.6 %/°C (T > 20 °C)

In the case of encapsulated devices, J_{sc} remains almost constant in the investigated temperature range. The deterioration of J_{sc} can be due to decreasing photocurrent, increasing shunt resistance, and increasing interfacial charge recombination. Whereas better charge extraction and hence carrier collection rates would improve J_{sc}. The final balance of all these mechanisms will then determine the trend of the short-circuit current density.

Concerning the power conversion efficiency η, the minimal value for the temperature coefficient of the efficiency derived in the thermodynamic limit of detailed balance is -0.13%/K.[41] We note, that in several cases a nonlinear thermal coefficient has been reported[40], which was attributed to the use of the hole-transporting material Spiro-OMeTAD and its corresponding low glass transition temperature.[39] In contrast to other types of solar cells and as a general observation on PSCs, the *FF* increases with temperature due to the fast decrease of the V_{oc} while the J_{sc} remains constant.

In Fig. S11 in the SI, we present the interpolated empirical matrix of power conversion efficiency as a function of the cell temperature and the total irradiance obtained for two PSC structures: (PSC_A) Glass/ FTO/ TiO_2 /triple-cation perovskite/ Spiro-OMeTAD /Au /Glass (from this work) and (PSC_B) Glass/ITO/MeO-2PACz/triple-cation perovskite/C_{60}/SnO_2/Cu (data taken from ref. [41]). The main difference is the non-linearity of the power conversion efficiency obtained for the structure PSC_A, probably due to the use of Spiro-OMeTAD. This data matrix will enable us to estimate the power output of the solar cell under different operating temperatures and irradiation intensities.

4. Simulations

In this section, we apply our model to evaluate the cell temperature of a stable glass-PSC-glass sample configuration under different realistic meteorological conditions assuming no degradation of the perovskite. In section 4.1, we also estimate the different thermal exchanges that take place in a PSC during one complete day. In section 4.2, we present the applicability of our model to calculate the Nominal Operating Cell Temperature (NOCT), which is the temperature reached by the cells of the PV module under normal operating conditions. Finally, in section

4.3, we study the effect of the thermal model on the estimated EY in different geographical locations.

4.1 Calculation of the cell temperature.

First, we compared our model with the empirical approaches provided by Tress et al.[40] and Jošt et al. [41] (see Section S1.1 in the SI). From this comparison, except in limited specific conditions, we see the evolution of the cell temperature not to be the same as the one obtained from our model which considers a more realistic nonlinear relation among the cell temperature, ambient temperature, and direct irradiance. In addition, in section S2.1 in the SI, our model reproduces experimental transient data confirming its validity and also showing the potential of using this model to interpret the performance of PSCs under realistic conditions.

thermal parameters used in these simulations for PSC_A and PSC_B are enclosed in Table 1 in section S3.4 in the SI. In this table, we included the percentage of the absorbed irradiance by each layer which will impact on the increasing of the device temperature. The irradiance on the PSC_A and PSC_B structures is mainly absorbed by the glass/FTO (18 %) and perovskite (45.5 %) and by the glass/ITO (10 %) and perovskite (46.5 %) layers, respectively. As both absorptions on the perovskite are quite similar, if we assume the same efficiency, the device A will achieve higher temperature than device B under the same conditions due to a higher thermal absorption loss. Moreover, in this case, PSC_B exhibits a higher efficiency, thus, its operational cell temperature is lower than the one for PSC_A. In addition, PSC_A is more temperature-sensitive due to the higher

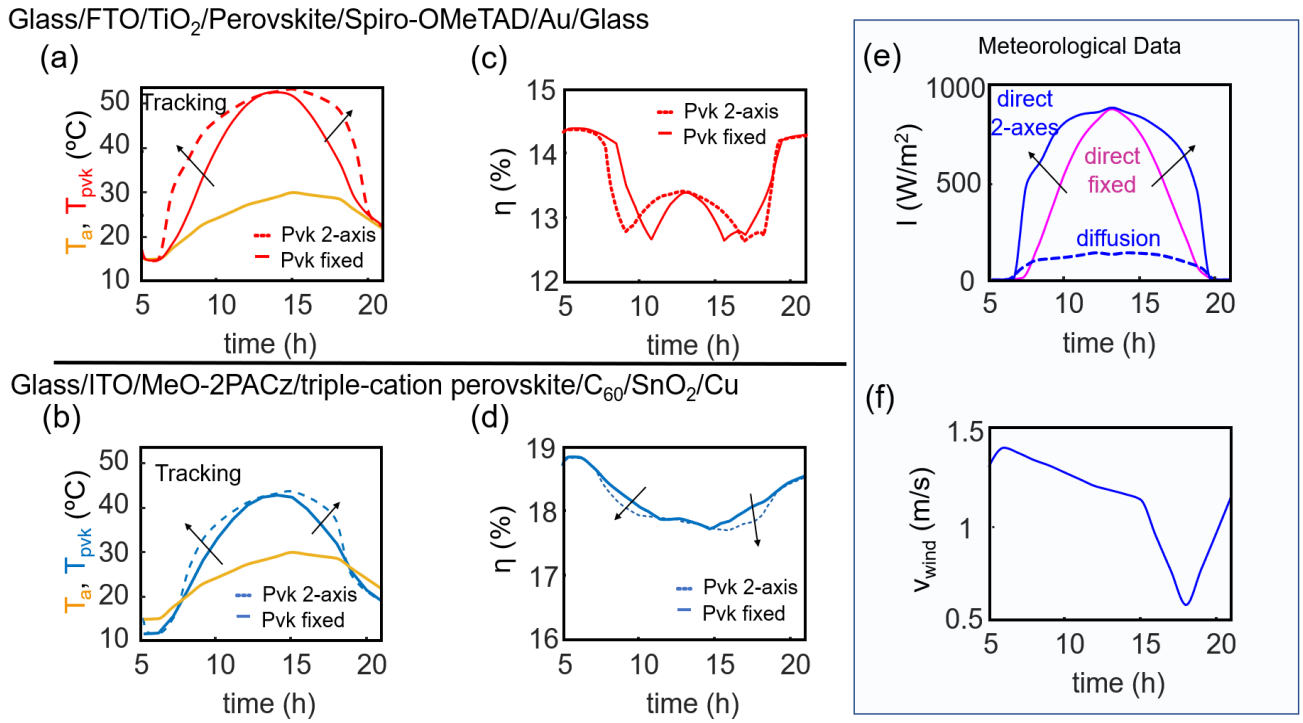

FIGURE. 4. (A) AND (B) SIMULATED EVOLUTION OF THE CELL TEMPERATURE OVER THE COURSE OF ONE DAY OF TWO STABLES PSCS BOTH LOCATED IN A MODULE WITH 2-AXIS AND A FIXED MODULE AT 37° (OPTIMUM ANGLE FOR BORDEAUX) ON AN ARBITRARY DAY IN AUGUST OF A TYPICAL YEAR IN BORDEAUX (TMY). THE STRUCTURES ARE (A) GLASS/FTO/TIO$_2$/DOUBLE-CATION PEROVSKITE/SPIRO-OMETAD/AU/GLASS AND (B)GLASS/ITO/MEO-2PACZ/TRIPLE-CATION PEROVSKITE/C$_{60}$/SNO$_2$/CU. THEIR CORRESPONDING EFFICIENCIES ARE PLOTTED IN FIGURE (C) AND (D). THE RECORDED ENVIRONMENTAL PARAMETERS IN BORDEAUX ARE: (A) AMBIENT TEMPERATURE T$_a$ (E) DIFFUSE IRRADIANCE AND DIRECT IRRADIANCE CORRECTED FOR

Importantly, our model allows us to calculate the contribution of the absorption, conduction, radiation and convection at any given time of the day and to study which layers of the device will induce a greater temperature increase in the solar cell. In Fig. 4 we present the estimated evolution of the cell temperature of two different PSCs in a fixed module and 2-axis tracking module under the meteorological data recorded on an arbitrary day in August of a typical year in Bordeaux. In Fig. 4(a)-(c) the simulated structure is (PSC_A) Glass/FTO/TiO_2/Perovskite/Spiro-OMeTAD/Au/Glass, and for Fig. 4(b)-(d), the structure is (PSC_B) Glass/ITO/MeO-2PACz/Perovskite/C_{60}/SnO_2/Cu. The electrical performances of PSC_A and PSC_B are modelled by the empirical efficiency matrix represented in Fig. S11c and S11b in the SI, respectively. The dependence of the efficiency with temperature and irradiance intensity. The input meteorological data are represented in Fig. 4: (a) ambient temperature, (e) direct and diffuse irradiance corrected for one module tilted at 37° (optimum angle for Bordeaux) and for a 2-axis tracking module, and (f) wind speed corrected for an altitude of 2 m above ground level. From Fig. 4(a) and (b), we observe that the temperature in the 2-axis tracking module is higher than the one obtained in a fixed module, which is related to the higher direct irradiation (Fig. 4(e)). This gap in temperature values can reach up to of 10 °C in the case of PSC_A.

In Fig. 5, we show the evolution of the conduction (cd), convection (cv), absorption (incident input flux) and radiation (rad) contributions as a function of the time for the simulation

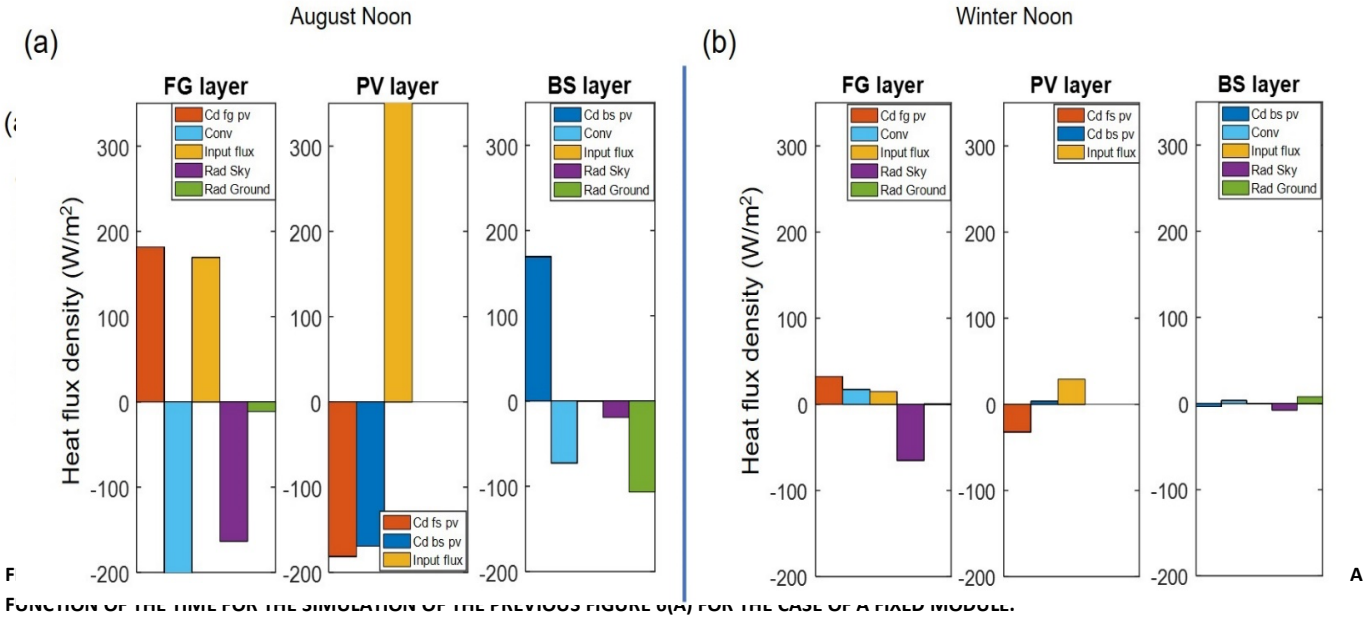

F A
FUNCTION OF THE TIME FOR THE SIMULATION OF THE PREVIOUS FIGURE 3(A) FOR THE CASE OF A FIXED MODULE.

FIGURE. 5 CONDUCTION (CD), CONVECTION (CONV) AND RADIATION (RAD) CONTRIBUTION AT NOON IN AN ARBITRARY IN AUGUST AND IN JANUARY IN A TYPICAL YEAR IN BORDEAUX FOR A FIXED MODULE IN A PV FARM.: (A) I_B = 867 W/M^2, I_{DIFF} = 136 W/M^2 T_{AMB} = 22.9 °C, V_{W10} = 1.7 M/S, T_{CELL} = 44 °C. (B) I_B = 31 W/M^2, I_{DIFF} = 75 W/M^2 T_{AMB} = 5.1 °C, V_{W10} = 1.12 M/S, T_{CELL} = 3 °C.

of PSC_A. The input fluxes absorbed in the perovskite layer and in the Glass/FTO are the main mechanisms that increase the temperature of the cell, as it is to expect from the absorbed percentages in Table 1 in section S3.4 in the SI. Interestingly, different glass materials present different absorption profiles, that impacts strongly on the thermal losses, without affecting the absorption of the perovskite layer (see Figure S17 in the SI). We note, that while our simulations do not consider cell degradation directly, our model nonetheless identifies heat sinks in the device stack, which eventually accelerate ageing of the affected components. The convection also warms up the cell at night (20h–6h) while the convection in the day (7h-20h) contributes to the cooling of the system, due to a positive (night) or negative (day) difference between the ambient temperature and the FG (or BG) layers. The radiative exchanges will decrease the temperature of the cell all day and night. At lower irradiations (such as at dawn, dusk or cloudy-cold winter days) and at night, the radiative exchanges will promote the cell temperature to be lower than the ambient temperature. In Fig. S14 in the SI, we comprehensively compare the thermal contributions at (a) 8 am and (b) 12 pm on an arbitrary day of August in Bordeaux. In the morning, the radiative exchange due to the low sky temperature is the most significant contribution to the cooling of the system. The convection contribution is higher at noon due to the increase of the wind speed and the larger temperature difference between the ambient and the solar cell.

In Fig. 6, we compare one typical thermal contribution at noon in August and in January. First, there is a clear difference for all the different contributions. In winter, due to the low ambient temperature, the cell is working at higher efficiency than in summer. In addition, as the thermal flux absorbed by the perovskite layer is low, the cell temperature can be even lower than the ambient temperature. In that case, the input flux absorbed in the perovskite layer is similar to the input flux absorbed in the front glass/FTO layer. The convection can even contribute to heating the cell up to the ambient temperature.

4.2 Nominal Operating Cell Temperature (NOCT).

The NOCT is the temperature reached by the cell under the following operating conditions: (i) 800 W/m^2 irradiation, (ii) ambient temperature of 20 °C and (iii) wind velocity of 1 m/s[7]. It is used to compare PV modules and to estimate the cell temperature through empirical functions of irradiance intensity and wind velocity. The better performing modules present lower NOCT. The lower the cell temperature of the module, the more power will be delivered. In section S3.2 in the SI, we apply our model to estimate the NOCT of a module situated in a PV farm and a module on a rooftop in Bordeaux. From these simulations, we observe a 6 °C increase of NOCT when the module is installed on a rooftop (42 °C) instead of a PV farm installation (36°C).

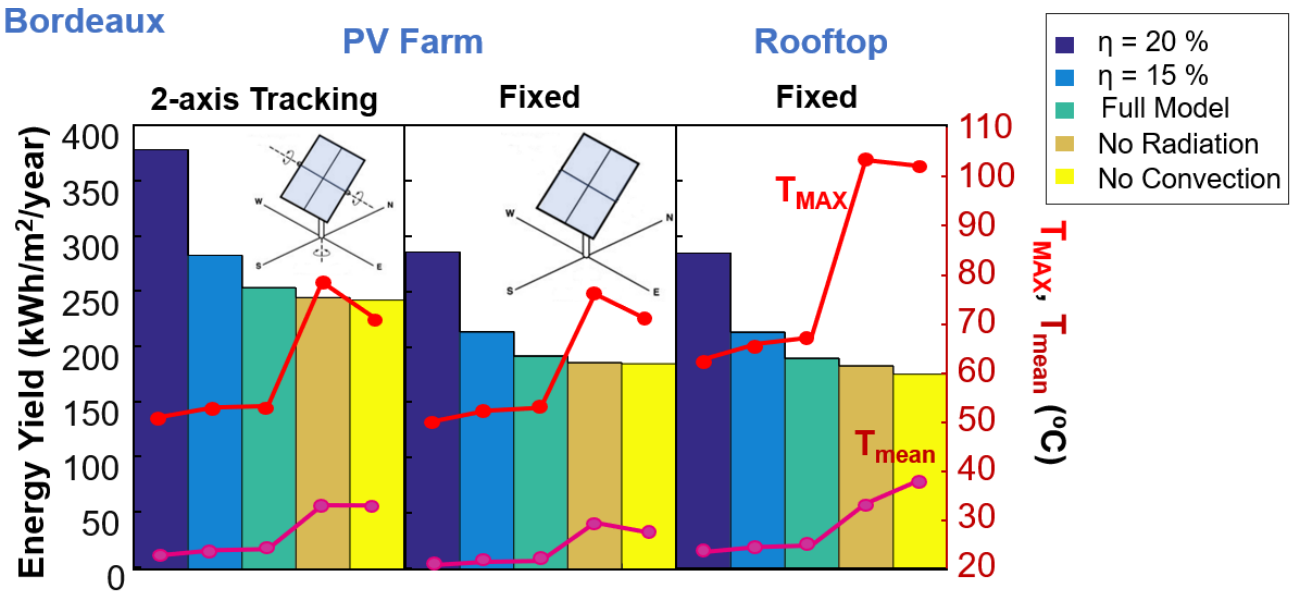

FIGURE. 7. ANNUAL ENERGY YIELD PRODUCTION CALCULATED IN BORDEAUX (FRANCE) FOR FOUR DIFFERENT STABLE SOLAR CELLS UNDER THREE DIFFERENT CONFIGURATIONS. DIFFERENT SOLAR CELLS: (1) THE CELL HAS AN EFFICIENCY OF 20 % AT 20 °C (TEMPERATURE COEFFICIENT: -0.13 %/K); (2) THE CELL HAS AN EFFICIENCY OF 15 % AT 20 °C (TEMPERATURE COEFFICIENT: -0.13 %/K); (3) STRUCTURE (A) GLASS/FTO/TiO_2/PEROVSKITE/SPIRO-OMETAD/AU/GLASS -WE CONSIDER THE COMPLETE MODEL, ALL THE DIFFERENT THERMAL MECHANISMS-; (4) THE CASE (3) WITHOUT CONSIDERING THE CONVECTION CONTRIBUTION; AND (5) THE CASE (3) WITHOUT CONSIDERING THE RADIATIVE EXCHANGES. CELLS ARE SIMULATED UNDER TWO DIFFERENT MODULE CONFIGURATIONS (FIXED AND 2-AXIS TRACKING) AND FOR TWO DIFFERENT PLACES IN THE ROOFTOP OR IN A PV FARM, LOCATED IN BORDEAUX

4.3 Calculation of annual energy production

The annual energy yield (EY) is conventionally referred to as the output energy produced by a PV system for one year (Wh/m²/year). We consider that the cells are working at MPP all time. In PV modules, the MPPT (maximum power point tracking) is used to adapt the load to get maximum efficiency. One of the consequences is that the cell temperature at MPP is lower than at other current-voltage operating points[68]. The reason is that the output power is higher at MPP, therefore, less of the remaining input power will contribute to an increase of the cell temperature.

In addition, these predictions represent the maximum EY obtained from a PV module considering its intrinsic dependence with the temperature and light intensity. In this approach, we do not consider irreversible degradation due to temperature stress observed in the literature[40, 41, 43]. In the last years, important progress has been made in the improvement of perovskite device stability[29, 46, 73]. More information about the thermal degradation of PSCs and the impacts on its EY and lifetime is included in section S4 in the SI.

We have calculated the EY, the average operational temperature and the maximum temperature achieved for two different module configurations (fixed and 2-axis tracking) and for two different applications, on a rooftop or in a PV farm, located in Bordeaux (France). In addition, we considered five different scenarios: (1) a cell with an efficiency of 20 % at 20 °C and temperature coefficient of -0.13 %/K; (2) a cell with an efficiency of 15 % at 20 °C and temperature coefficient of -0.13 %/K; (3) our cell layout PSC_A working with the empirical efficiency matrix (see. Fig. S11(b) in the SI) and taking into account absorption, convection, conduction and radiation in the thermal module (denoted as Full Model); (4) similar to case (3) but excluding convection; and (5) similar to case (3) but excluding radiation. The cell with the higher efficiency works at a lower temperature and hence exhibits a higher EY. From Fig. 7, we also conclude that for the PSCs considered here, the EY delivered by a fixed module deployed in a PV farm is similar to the one on a rooftop. However, for the rooftop installation, the cells will work at a higher temperature, due to reduced thermal exchanges (almost adiabatic conditions) at the bottom side, as convection with a thin layer of air or conduction with the roof material can be neglected. This leads to fewer heat sinks, eventually resulting in faster degradation of the module performance. The cell temperature can reach up to 100°C on a rooftop if the cell is not cooled down.

Finally, in Figure 8, we have calculated the EY for the PSC_A located in a PV farm in Paris (France), Bordeaux and Granada (Spain) under the following different scenarios: (1) considering all the mechanisms (absorption, conduction, convection, and radiation) with a constant efficiency of 15 %, (2) considering all the mechanisms with the empirical matrix of efficiencies, (3) excluding convection and (4) excluding radiation. In the case of Bordeaux, in Figure S13, we present the estimated evolution of the cell temperature for the case (2). In Fig. 8. Paris, Bordeaux and Granada represent the weather in the northern-to-middle and southern part of western Europe, with Paris and Bordeaux being windier than Granada. Granada, as the location with the highest irradiance in these examples, leads to the largest EY. Strikingly, the plots show the importance of considering a realistic thermal-dependent efficiency instead of a constant efficiency. The relative difference in EY between the simulations with and without a realistic thermal model amounts to 11 %, 12 % and 13 % for Paris, Bordeaux and Granada, respectively, which are similar to the range of values (between 10 % and 13 %) obtained for other places in Europe (see section S3.3 in SI). We note that the thickness of the glass layers slows down the

response of the solar cell to changes in the weather, implying modification in the final EY. In the simulation, this effect is observed when the time step of the recorded meteorological data is significant to the thermal response time (every 5 min). In particular convection and radiation are important for the calculation of the EY. Therefore, neglecting these two contributions could lower the EY by over 4% in our example. The cell temperature would be higher if any of the convection or the radiation exchanges are suppressed. This effect becomes more pronounced in places of highest irradiation, such as Granada, in which the cooling of the system due to radiation and convection is essential. In these places, it is crucial to decrease absorption losses in the glass and FTO layers to reduce the operational cell temperature which will reduce device degradation and improve device stability.

Conclusions

In this work, we show the importance of considering the thermal contributions in the calculation of the energy yield of perovskite solar cells, by applying an optical-electrical-thermal model to simulate the devices under realistic meteorological conditions even without taking further device degradation into account. The model is composed of a thermal transient RC circuit module, used to predict the cell temperature, and by the electrical performance of the PSCs as a function of device parameters and environmental variables. The thermal model is linked with the thermal-optical dependence of the electrical performance through experimental measurements of current-voltage parameters as function of temperature and light intensity. To do that, we propose a protocol based on the transient thermal response mainly driven by the thicknesses of the glass.

From the model, we find the cell temperature to be strongly linked to the absorbed power which is not converted to electricity in the perovskite layer (maximum of 45.5-50 % of the total input irradiation), in the front glass (9.1 %) and in the FTO (9.3 %) layer. In places of high irradiance, the absorption in glass, FTO and the perovskite layer will be a source of heat increasing the cell temperature. Therefore, the model allows to detect what are the most sensible layers which will contribute to increasing the cell temperature.

We have shown the applicability of our model to predict the NOCT for a given location depending on the type of installation (fixed module in a PV farm or on a rooftop). Under the simulated conditions in this work, the type of installation can modify the NOCT up to 6 °C. The refined modelling of the thermal properties of the cell has distinct implications on the annual energy yield. We find the EY of PSC modules, in PV farms and on rooftops, in different geographical locations to be dependent on radiative exchanges and air convection mechanism. The difference in EY between using a standard model and considering our realistic thermal model amounts to minus 10 %-13 % for different places in Europe. In addition, modules in rooftop installations exhibit fewer heatsinks than their counterparts in PV farms and hence would suffer from faster degradation rates.

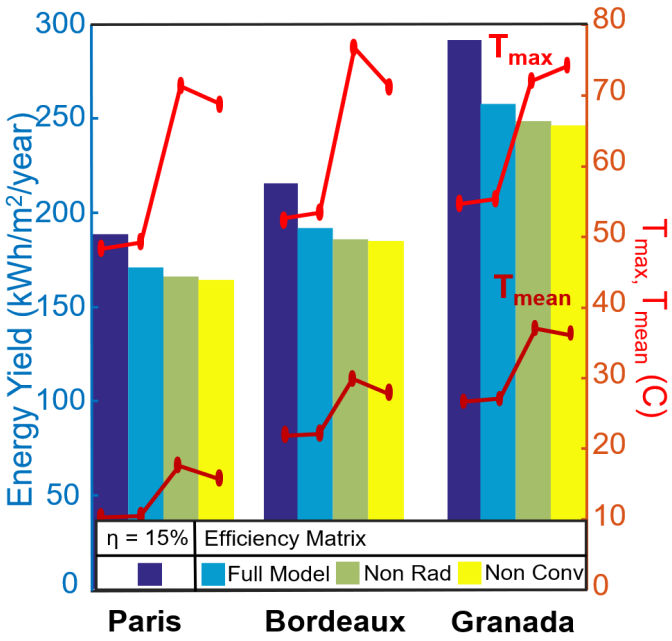

FIGURE. 8 ANNUAL ENERGY YIELD PRODUCTION CALCULATED IN PARIS, BORDEAUX (FRANCE) AND GRANADA (SPAIN) FOR A PSC IN A PV FARM UNDER DIFFERENT CONSIDERATIONS: (1) ALL THE MECHANISMS (CONDUCTION, CONVECTION AND RADIATION) AND A CONSTANT EFFICIENCY OF 15 %, (2) ALL THE MECHANISMS AND THE EMPIRICAL MATRIX OF EFFICIENCIES, (3) WITHOUT CONVECTION AND THE EMPIRICAL MATRIX OF EFFICIENCIES AND (4) WITHOUT RADIATION AND THE

Our results underline that management of the thermal load is critical for maximizing the performance of perovskite solar cells and increasing the module lifetime. Finally, it should be noted that this thermal model can also be applied to evaluate the lifetime of perovskite PV modules[43], EY or to evaluate the impact of the temperature on the levelized cost of energy LCOE[56].

Conflicts of interest

There are no conflicts to declare.

Contributions

Conceptualization, P.L.-V., J.-B.P.; Methodology, P.L.-V, J.-B.P., M.A.; Software, P-L.-V. (thermal model/energy yield calculation/all the figures); Discussion on programming P-L.-V., M.A. and J.-B.P.; Software (optical simulation) J.-B.P and A.J.; Validation, P-L.-V., M.A.; Formal Analysis (simulations), P.L.-V., J.-B.P, M. A., J.-F.G; Design of Experiments, P.L.-V., M. A., J.-F.G., and S.C.; Perform the experiments P.L.-V., M. A., S.C and M. J.; Formal Analysis (experiments), P.L.-V., J.-B.P, M. A., S.C, J.R., J.F.G., P.S.; Resources (device fabrication), A.Y., M. J. and J.R., Resources (installations) M. A., J.R.; Investigation, P.L.-V., J.-B.P., M. A., P.S., J.F.G.; Data Curation, P.L.-V.; Writing - Original Draft, P.L-V.; Review & Editing, P.L.-V., P.S., J.-B.P., S.C., J.R., A.J. M.A., J.-F.G; Visualization, P.-L.V., P.S., M.A., J.-B.P..

Acknowledgements

This project has been supported by the French Government in the frame of the program of investment for the future (Programme d'Investissement d'Avenir – ANR-IEED-002-01). S.C. would like to thank funding from the European Union's Horizon 2020 research and innovation programme under the Marie Skłodowoska-Curie Grant Agreement N 845612. P.S. thanks the French Agence Nationale de la Recherche for funding under the contract number ANR-17-MPGA-0012.

References

1. P. Lopez-Varo, J. A. Jiménez-Tejada, M. García-Rosell, S. Ravishankar, G. Garcia-Belmonte, J. Bisquert and O. Almora, *Advanced Energy Materials*, 2018, **8**, 1702772-1702772.
2. F. Staub, I. Anusca, D. C. Lupascu, U. Rau and T. Kirchartz, *J. Phys. Mater.*, 2020, **3**, 025003-025003.
3. J. Gong, S. B. Darling and F. You, *Energy & Environmental Science*, 2015, **8**, 1754-5692.
4. S. G. Motti, D. Meggiolaro, S. Martani, R. Sorrentino, A. J. Barker, F. De Angelis and A. Petrozza, *Advanced Materials*, 2019, **31**, 1901183.
5. W. Tress, *Advanced Energy Materials*, 2017, **7**.
6. M. V. Khenkin, E. A. Katz, A. Abate, G. Bardizza, J. J. Berry, C. Brabec, F. Brunetti, V. Bulović, Q. Burlingame, A. Di Carlo, R. Cheacharoen, Y. B. Cheng, A. Colsmann, S. Cros, K. Domanski, M. Dusza, C. J. Fell, S. R. Forrest, Y. Galagan, D. Di Girolamo, M. Grätzel, A. Hagfeldt, E. von Hauff, H. Hoppe, J. Kettle, H. Köbler, M. S. Leite, S. Liu, Y. L. Loo, J. M. Luther, C. Q. Ma, M. Madsen, M. Manceau, M. Matheron, M. McGehee, R. Meitzner, M. K. Nazeeruddin, A. F. Nogueira, Ç. Odabaşı, A. Osherov, N. G. Park, M. O. Reese, F. De Rossi, M. Saliba, U. S. Schubert, H. J. Snaith, S. D. Stranks, W. Tress, P. A. Troshin, V. Turkovic, S. Veenstra, I. Visoly-Fisher, A. Walsh, T. Watson, H. Xie, R. Yıldırım, S. M. Zakeeruddin, K. Zhu and M. Lira-Cantu, *Nature Energy*, 2020, **5**, 35-49.
7. K. Domanski, A. Hagfeldt, M. Graetzel and W. Tress, *Nature Energy*, 2018, **3**, 61-67.
8. A. M. Gracia-Amillo, G. Bardizza, E. Salis, T. Huld and E. D. Dunlop, *Renewable and Sustainable Energy Reviews*, 2018, **93**, 76-89.
9. M. Mussard and M. Amara, *Solar Energy*, 2018, **174**, 409-421.
10. G. Notton, C. Cristofari, M. Mattei and P. Poggi, *Applied Thermal Engineering*, 2005, **25**, 2854-2877.
11. J. You, L. Meng, T. B. Song, T. F. Guo, W. H. Chang, Z. Hong, H. Chen, H. Zhou, Q. Chen, Y. Liu, N. De Marco and Y. Yang, *Nature Nanotechnology*, 2016, **11**, 75-81.
12. D. Bryant, N. Aristidou, S. Pont, I. Sanchez-Molina, T. Chotchunangatchaval, S. Wheeler, J. R. Durrant and S. A. Haque, *Energy and Environmental Science*, 2016, **9**, 1655-1660.
13. J. A. Christians, P. A. Miranda Herrera and P. V. Kamat, *Journal of the American Chemical Society*, 2015, **137**, 1530-1538.
14. G. Divitini, S. Cacovich, F. Matteocci, L. Cinà, A. Di Carlo and C. Ducati, *Nature Energy*, 2016, **1**.
15. R. L. Milot, G. E. Eperon, H. J. Snaith, M. B. Johnston and L. M. Herz, *Advanced Functional Materials*, 2015, 6218-6227.
16. H. Baig, H. Kanda, A. M. Asiri, M. Khaja Nazeeruddin and T. Mallicka, *Sustainable Energy & Fuels*, 2020, **4**, 528-537
17. J. A. Schwenzer, L. Rakocevic, R. Gehlhaar, T. Abzieher, S. Gharibzadeh, S. Moghadamzadeh, A. Quintilla, B. S. Richards, U. Lemmer and U. W. Paetzold, *ACS Applied Materials & Interfaces*, 2018, **10**, 16390-16399.
18. J. A. Schwenzer, L. Rakocevic, T. Abzieher, D. Rueda-delgado, S. Moghadamzadeh, S. Gharibzadeh, I. M. Hossain, R. Gehlhaar, B. S. Richards, S. Member, U. Lemmer and U. W. Paetzold, *IEEE Journal of Photovoltaics*, 2020, 1-8.
19. Y. Han, S. Meyer, Y. Dkhissi, K. Weber, J. M. Pringle, U. Bach, L. Spiccia and Y. B. Cheng, *Journal of Materials Chemistry A*, 2015, **3**, 8139-8147.
20. O. Dupré, B. Niesen, S. De Wolf and C. Ballif, *Journal of Physical Chemistry Letters*, 2018, **9**, 446-458.
21. M. T. Hörantner and H. J. Snaith, *Energy and Environmental Science*, 2017, **10**, 1983-1993.
22. J. Lehr, M. Langenhorst, R. Schmager, S. Kirner, U. Lemmer, B. S. Richards, C. Case and U. W. Paetzold, *Sustainable Energy & Fuels*, 2018, **2**, 2754.
23. R. Hosseinian Ahangharnejhad, A. B. Phillips, K. Ghimire, P. Koirala, Z. Song, H. M. Barudi, A. Habte, M. Sengupta, R. J. Ellingson, Y. Yan, R. W. Collins, N. J. Podrazaa and M. J. Heben, *Sustainable Energy Fuels* 2019, **3**, 1841-1851.
24. M. Jost, E. Köhnen, A. B. Morales-vilches, B. Lipovsek, K. Jäger, B. Macco, A. Al-Ashouri, J. Krc, L. Korte, B. Rech, R. Schlatmann, M. Topic, B. Stannowski and S. Albrecht, *Energy and Environmental Science*, 2018, **11**, 3511-3523.
25. O. Dupré, R. Vaillon and M. A. Green, *Thermal Behavior of Photovoltaic Devices*, Springer, 2017.
26. H. Zhang, X. Qiao, Y. Shen, T. Moehl, S. M. Zakeeruddin, M. Grätzel and M. Wang, *Journal of Materials Chemistry A*, 2015, **3**, 11762-11767.
27. T. J. Jacobsson, W. Tress, J. P. Correa-Baena, T. Edvinsson and A. Hagfeldt, *Journal of Physical Chemistry C*, 2016, **120**, 11382-11393.
28. W. L. Leong, Z. E. Ooi, D. Sabba, C. Yi, S. M. Zakeeruddin, M. Graetzel, J. M. Gordon, E. A. Katz and N. Mathews, *Advanced Materials*, 2016, **28**, 2439-2445.
29. T. T. Ava, A. Al Mamun, S. Marsillac and G. Namkoong, *Applied Sciences (Switzerland)*, 2019, **9**.
30. A. Bruno, D. Cortecchia, X. Y. Chin, K. Fu, P. P. Boix, S. Mhaisalkar and C. Soci, *Advanced Energy Materials*, 2017, **7**, 1-9.
31. Y. Yuan and J. Huang, *Accounts of Chemical Research*, 2016, **49**, 286-293.
32. E. Aydin, T. G. Allen, M. De Bastiani, L. Xu, J. Ávila, M. Salvador, E. Van Kerschaver and S. De Wolf, *Nature Energy*, 2020, **5**, 851-859.
33. M. A. Green, Y. Jiang, A. M. Soufiani and A. Ho-Baillie, *Journal of Physical Chemistry Letters*, 2015, **6**, 4774-4785.

34. L. K. Ono, S. R. Raga, S. Wang, Y. Kato and Y. Qi, *Journal of Materials Chemistry A*, 2015, **3**.
35. X. Wang, J. Wu, Y. Yang, X. Liu, Q. Guo, Z. Song, G. Li, Z. Lan and M. Huang, *Journal of Materials Chemistry A*, 2019, **7**, 13256-13264.
36. T. H. Schloemer, J. A. Christians, J. M. Luther and A. Sellinger, *Chemical Science*, 2019, **10**, 1904-1935.
37. M. Jeong, I. W. Choi, E. M. Go, Y. Cho, M. Kim, B. Lee, S. Jeong, Y. Jo, H. W. Choi, J. Lee, J.-H. Bae, S. K. Kwak, D. S. Kim and C. Yang, *Science*, 2020, **369**, 1615-1620.
38. T. Malinauskas, D. Tomkute-Luksiene, R. Sens, M. Daskeviciene, R. Send, H. Wonneberger, V. Jankauskas, I. Bruder and V. Getautis, *ACS Applied Materials & Interfaces*, 2015, **7**, 11107-11116.
39. A. K. Jena, Y. Numata, M. Ikegami and T. Miyasaka, *Journal of Materials Chemistry A*, 2018, **6**, 2219-2230.
40. W. Tress, K. Domanski, B. Carlsen, A. Agarwalla, E. A. Alharbi, M. Graetzel and A. Hagfeldt, *Nature Energy*, 2019, **4**, 568-574.
41. M. Jošt, B. Lipovšek, B. Glažar, A. Al-Ashouri, K. Brecl, G. Matič, A. Magomedov, V. Getautis, M. Topič and S. Albrecht, *Advanced Energy Materials*, 2020, **10**, 2000454.
42. K. Domanski, B. Roose, T. Matsui, M. Saliba, S. H. Turren-Cruz, J. P. Correa-Baena, C. R. Carmona, G. Richardson, J. M. Foster, F. De Angelis, J. M. Ball, A. Petrozza, N. Mine, M. K. Nazeeruddin, W. Tress, M. Grätzel, U. Steiner, A. Hagfeldt and A. Abate, *Energy and Environmental Science*, 2017, **10**, 604-613.
43. J. P. Bastos, G. Uytterhoeven, W. Qiu, U. W. Paetzold, D. Cheyns, S. Surana, J. Rivas, M. Jaysankar, W. Song, T. Aernouts, J. Poortmans and R. Gehlhaar, *ACS Applied Materials & Interfaces*, 2019, **11**, 16517-16526.
44. S. Kim, S. Bae, S. W. Lee, K. Cho, K. D. Lee, H. Kim, S. Park, G. Kwon, S. W. Ahn, H. M. Lee, Y. Kang, H. S. Lee and D. Kim, *Scientific Reports*, 2017, **7**, 1-9.
45. Y. Huang, P. Lopez-Varo, B. Geffroy, H. Lee, J.-E. Bourée, A. Mishra, P. Baranek, A. Rolland, L. Pedesseau, J.-M. Jancu, J. Even, J.-B. Puel and M. Gueunier-Farret, *Journal of Photonics for Energy*, 2020, **10**, 024502.
46. C. C. Boyd, R. Cheacharoen, T. Leijtens and M. D. McGehee, *Chemical Reviews*, 2019, **119**, 3418-3451.
47. Photovoltaic Geographical System of the European Commission https://re.jrc.ec.europa.eu/pvg_tools/fr/tools.html).
48. A. Julien, J.-B. Puel, P. Lopez-Varo, J.-F. Guillemoles and S. Collin, *Opt. Express*, 2020, **28**, 37487-37504.
49. E. Raoult, R. Bodeux, S. Jutteau, S. Rives, A. Yaiche, D. Coutancier, J. Rousset and S. Collin, presented in part at the 36th European Photovoltaic Solar Energy Conference and Exhibition (EU PVSEC), 2019, 2019.
50. R. Gehlhaar, T. Merckx, W. Qiu and T. Aernouts, *Global Challenges*, 2018, **2**, 1800008.
51. A. D. Jones and C. P. Underwood, *Solar Energy*, 2001, **70**, 349-359.
52. E. Skoplaki and J. A. Palyvos, *Renewable Energy*, 2009, **34**, 23-29.
53. O. Dupré, R. Vaillon and M. A. Green, *Solar Energy Materials and Solar Cells*, 2015, **140**, 92-100.
54. L. Weiss, M. Amara and C. Ménézo, *Prog. Photovolt: Res. Appl.*, 2016, **24**, 12-27.
55. M. Sahli, J. P. M. Correia, S. Ahzi and S. Touchal, *Solar Energy Materials and Solar Cells*, 2018, **180**, 358-372.
56. L. Xu, W. Liu, H. Liu, C. Ke, M. Wang, C. Zhang, E. Aydin, M. Al-Aswad, K. Kotsovos, I. Gereige, A. Al-Saggaf, A. Jamal, X. Yang, P. Wang, F. Laquai, T. G. Allen and S. De Wolf, *Joule*, 2021, **5**, 631-645.
57. R. Couderc, M. Amara and M. Lemiti, *IEEE Journal of Photovoltaics*, 2016, **6**, 1123-1131.
58. E. Kaplani and S. Kaplanis, *Solar Energy*, 2014, **107**, 443-460.
59. J. Allan, H. Pinder and Z. Dehouche, *AIP Advances*, 2016, **6**, 035011.
60. M. Hammami, S. Torretti, F. Grimaccia and G. Grandi, *Applied Sciences*, 2017, **7**, 1107.
61. Thermal Coefficients: https://thermtest.com/materials-database).
62. Database: Density of Solids, Mineral Density: https://www.engineeringtoolbox.com/density-solids-d_1265.html).
63. Z. Y. Banyamin, P. J. Kelly, G. West and J. Boardman, *Coatings*, 2014, **4**, 732-746.
64. A. Pisoni, J. Jaćimović, O. S. Baris, M. Spina, R. Gaa, L. Forró and E. Horváth, *J. Phys. Chem. Lett.* , 2014, **5**, 2488-2492.
65. T. A. Tyson, W. Gao, Y. Chen, S. Ghose and Y. Yan, *Scientific Reports*, 2017, **7**, 9401-9401.
66. H. Zhang and J. W. Brill, *Journal of Applied Physics*, 2013, **114**, 1-9.
67. Ossila. Material Properties, https://www.ossila.com/products/fto-glass-unpatterned?variant=21518956481).
68. B.-G. Lohan, M. Amara, A. Kaminski-Cachopo and M. Lemiti, *Solar Energy Materials and Solar Cells*, 2018, **183**, 300-306.
69. F. Matteocci, L. Cinà, E. Lamanna, S. Cacovich, G. Divitini, P. A. Midgley, C. Ducati and A. Di Carlo, *Nano Energy*, 2016, **30**, 10.
70. M. A. Green, *Prog. Photovolt: Res. Appl.*, 2003, **11**, 333-340.
71. F. Ebadi, M. Aryanpour, R. Mohammadpour and N. Taghavinia, *Scientific Reports*, 2019, **9**, 1-9.
72. F. Fu, T. Feurer, Thomas P. Weiss, S. Pisoni, E. Avancini, C. Andres, S. Buecheler and Ayodhya N. Tiwari, *Nature Energy*, 2016, **2**.
73. L. Shi, M. P. Bucknall, T. L. Young, M. Zhang, L. Hu, J. Bing, D. S. Lee, J. Kim, T. Wu, N. Takamure, D. R. McKenzie, S. Huang, M. A. Green and A. W. Y. Ho-Baillie, *Science*, 2020, **368**, eaba2412.